

# Two-Dimensional Ultrathin C<sub>2</sub>N Nanosheets for High-Performance Sodium-Ion Storage

Tongtong Shang<sup>+, [a, b]</sup> Jinshu Zhang<sup>+, [a]</sup> Yantuo Li,<sup>[a]</sup> Yang Yang,<sup>[a]</sup> Jianxue Wu,<sup>[a]</sup> Mingyi Ning,<sup>[a]</sup> and Wei Liu<sup>\*[a, b]</sup>

In this study, we have created and investigated ultrathin, large-size two-dimensional C<sub>2</sub>N nanosheets, which serve as promising anode materials for sodium ion batteries. Those ultrathin C<sub>2</sub>N nanosheets were produced through a chemical vapor deposition process, involving the polymerization of the precursor molecule HAT-CN on sodium chloride templates. Notably, these nanosheets inherit an abundance of nitrogen sites from the precursor molecules, which are highly advantageous for sodium ion storage. In addition, the ultrathin nature of these nanosheets leads to significantly shorter ion transport pathways, enhancing their capacity for rapid ion storage compared to C<sub>2</sub>N

particles. As a result, the anode constructed using C<sub>2</sub>N nanosheets demonstrates a notably higher capacity of 335.1 mAh g<sup>-1</sup> at 0.5 A g<sup>-1</sup>, outperforming the 211.5 mAh g<sup>-1</sup> of C<sub>2</sub>N particles. Furthermore, it exhibits outstanding rate performance, achieving 255.4 mAh g<sup>-1</sup> at a current density of 2.0 A g<sup>-1</sup>, along with excellent cycle stability, maintaining a reversible capacity retention of 92.9% over 1500 cycles at 2.0 A g<sup>-1</sup>. This research introduces a novel approach to developing high-capacity anode materials for sodium storage by utilizing carbon nitride materials.

## Introduction

The extensive use of lithium-ion batteries (LIBs) has driven the growth of the clean energy industry, substantially enhancing the overall quality of life. Nevertheless, the limited availability of lithium resources has imposed constraints on further advancements. In contrast to lithium, sodium is abundantly distributed on earth and is more accessible for mining. Moreover, sodium ions exhibit similar physicochemical properties to lithium ions.<sup>[1–3]</sup> Consequently, sodium-ion batteries (SIBs) have acted as an appealing alternative to LIBs. SIBs operate on a comparable mechanism to LIBs, yet they face the challenge that the ionic radius of sodium ions is larger than that of lithium ions.<sup>[4]</sup> As a consequence, most anode materials designed for LIBs are not well-suited for use in SIBs.<sup>[5,6]</sup>

Currently, the main candidate materials for the anode of SIBs encompass a range of options, including carbon-based materials,<sup>[7,8]</sup> alloy materials,<sup>[9,10]</sup> metal oxides,<sup>[11,12]</sup> and organic materials.<sup>[13,14]</sup> Among these, carbon-based materials are regarded as the most promising candidates owing to their superior performance in lithium-ion batteries.<sup>[15–17]</sup> However,

when employing conventional graphite electrodes, the substantial ionic radius difference hinders the effective and reversible embedding and extraction of sodium ions between the layers of graphite.<sup>[18]</sup> Similarly, due to the lack of effective active sites, many carbon-based materials exhibit limited capacity and poor cycling performance for sodium ion storage.

Incorporating heteroatoms such as Boron (B),<sup>[19,20]</sup> Nitrogen (N),<sup>[21,22]</sup> Phosphorus (P),<sup>[23,24]</sup> Fluorine (F),<sup>[25]</sup> and Sulfur (S)<sup>[26,27]</sup> into carbon-based materials has been considered a promising approach to augment electronic conductivity and supply additional active sites to facilitate sodium ion transport and storage.<sup>[28–31]</sup> In particular, nitrogen-doped carbon-based materials have been widely researched and acquired promising electrochemical properties.<sup>[32–34]</sup> However, the uncertainty of nitrogen doping position and the complication of the doping process are crucial factors restricting to achievement of high capacity and cycling stability for SIBs anode. Hence, it becomes imperative to explore synthetic strategies that can effectively regulate the nitrogen doping quantity and the doping configuration.

C<sub>2</sub>N is a distinctive member of the Nitrogen-doped carbon family, distinguished by its rich composition of pyrazine rings, a well-defined covalent structure composing carbon and nitrogen, and a meticulously ordered pore structure.<sup>[35–37]</sup> This material has an abundance of nitrogen active sites capable of accommodating alkali metal ions. Moreover, the pore structure on the surface is favorable for ionic conduction and storage.<sup>[38]</sup> Nowadays, many theoretical studies have manifested that the monolayers of C<sub>2</sub>N containing nitrogen atoms exhibit strong interactions with sodium ions, resulting in a maximum theoretical capacity, that is 6 to 8 times that of graphite.<sup>[39,40]</sup> Recently, C<sub>2</sub>N/reduced graphene oxide (C<sub>2</sub>N/rGO) has been synthesized via a two-dimensional confinement incorporating in-situ growth. The introduction of rGO into C<sub>2</sub>N has exposed more

[a] T. Shang,<sup>+</sup> J. Zhang,<sup>+</sup> Y. Li, Y. Yang, J. Wu, M. Ning, Prof. W. Liu  
School of Physics, Key Laboratory of Quantum Materials and Devices of Ministry of Education, Frontiers Science Center for Mobile Information Communication and Security  
Southeast University  
Nanjing 211189, China  
E-mail: 101012931@seu.edu.cn

[b] T. Shang,<sup>+</sup> Prof. W. Liu  
Purple Mountain Laboratories  
Nanjing 211111, China

<sup>†</sup> These authors contributed equally to this work.

Supporting information for this article is available on the WWW under <https://doi.org/10.1002/batt.202300613>

active sites and improved conductivity, which is advantageous for sodium ion storage. As a result,  $\text{C}_2\text{N}/\text{rGO}$  exhibits a reversible capacity of  $304.3 \text{ mAh g}^{-1}$  at  $0.1 \text{ A g}^{-1}$  (300 cycles), and stable cycling properties.<sup>[41]</sup> The introduction of rGO induces the transformation of  $\text{C}_2\text{N}$  bulks into nanoflakes, which in turn improves ionic conduction and storage. Given the above, it is of interest to directly develop a controllable process to synthesize  $\text{C}_2\text{N}$  nanosheets for efficient sodium ion storage.

In this work, we demonstrate the fabrication of ultrathin  $\text{C}_2\text{N}$  nanosheets with a well-organized nanostructure by polymerizing precursor molecule HAT-CN on sodium chloride templates via the chemical vapor deposition method. These two-dimensional ultrathin ( $\sim 4 \text{ nm}$ )  $\text{C}_2\text{N}$  nanosheets offer an abundance of available nitrogen active sites and enhanced sodium ion accessibility, which greatly facilitates sodium ion transport and storage. In comparison to  $\text{C}_2\text{N}$  particles,  $\text{C}_2\text{N}$  nanosheets show exceptional sodium ion storage properties, with a reversible capacity of  $335.1 \text{ mAh g}^{-1}$  at  $0.5 \text{ A g}^{-1}$ , prominent rate performance of  $255.4 \text{ mAh g}^{-1}$  at  $2.0 \text{ A g}^{-1}$ , and excellent cycle stability over 1500 cycles.

## Results and Discussion

The fabrication process of  $\text{C}_2\text{N}$  nanosheets via chemical vapor deposition method is described in Figure 1a. Firstly, the precursor HAT-CN is homogeneously mixed with NaCl crystals, which serve as the templates and facilitate the sublimation of HAT-CN during heating. The mixture was heated from  $25^\circ\text{C}$  to  $550^\circ\text{C}$  at a rate of  $4^\circ\text{C min}^{-1}$  and then held at  $550^\circ\text{C}$  for

120 min under Argon atmosphere. HAT-CN sublimes and adsorbs on the whole surfaces of NaCl to form even coatings, which subsequently generate ultrathin  $\text{C}_2\text{N}$  nanosheets on NaCl. The resulting mixture was soaked in deionized water to remove NaCl. Then, the floating  $\text{C}_2\text{N}$  nanosheets were collected by filtration and washed thoroughly with deionized water. Finally,  $\text{C}_2\text{N}$  nanosheets were freeze-dried and used for characterizations.  $\text{C}_2\text{N}$  particles were synthesized by direct polycondensation of HAT-CN under the same reaction conditions without NaCl.

The  $\text{C}_2\text{N}$  nanosheets have been captured in SEM, as shown in Figure 1b, c. Owing to the templating effect of sodium chloride, the transverse size of  $\text{C}_2\text{N}$  nanosheets is commonly in the range of tens of micrometers.<sup>[42]</sup> Figure 1d shows the atomic force microscope (AFM) topography image of the homogeneous  $\text{C}_2\text{N}$  nanosheet. The  $\text{C}_2\text{N}$  nanosheet has highly uniform and ultra-thin characteristics. As indicated by the corresponding height profile, the thickness of the nanosheet monolayer is about  $4.0 \text{ nm}$ . The SEM images and the corresponding energy-dispersive spectroscopy (EDS) elemental mappings (Figure S2, Supporting Information (SI)) illustrate the homogeneous distribution of carbon and nitrogen in the  $\text{C}_2\text{N}$  nanosheets and  $\text{C}_2\text{N}$  particles.

As shown in Figure 2a, the broad peak centered at  $26.2^\circ$  for  $\text{C}_2\text{N}$  nanosheets in the X-ray diffraction (XRD) patterns is consistent with the characteristic (002) peak for  $\text{C}_2\text{N}$ .<sup>[43]</sup> The Brunauer-Emmett-Teller (BET) surface area of the  $\text{C}_2\text{N}$  nanosheets ( $68.105 \text{ m}^2 \text{ g}^{-1}$ ) is superior to  $\text{C}_2\text{N}$  particles ( $15.534 \text{ m}^2 \text{ g}^{-1}$ ), as depicted in Figure 2b and S4, SI.<sup>[41]</sup> The relatively larger specific surface area of  $\text{C}_2\text{N}$  nanosheets is

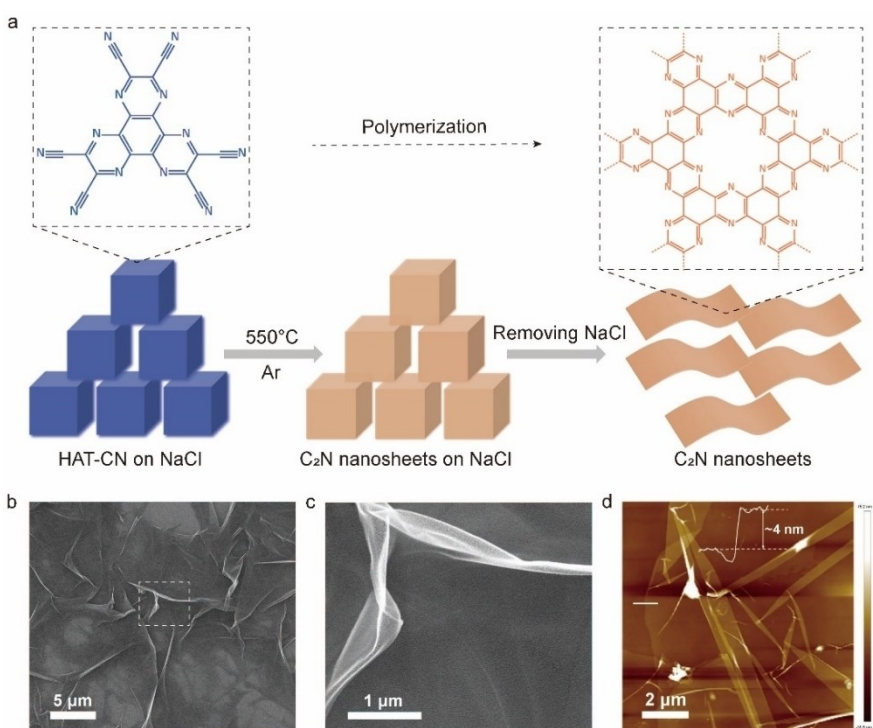


**Figure 1.** Synthesis and microscopic morphology of the  $\text{C}_2\text{N}$  nanosheets. a) Schematic illustration of the synthetic routes for the fabrication of  $\text{C}_2\text{N}$  nanosheets. b, c) SEM images of  $\text{C}_2\text{N}$  nanosheets. d) AFM topography image and height profiles of  $\text{C}_2\text{N}$  nanosheets.

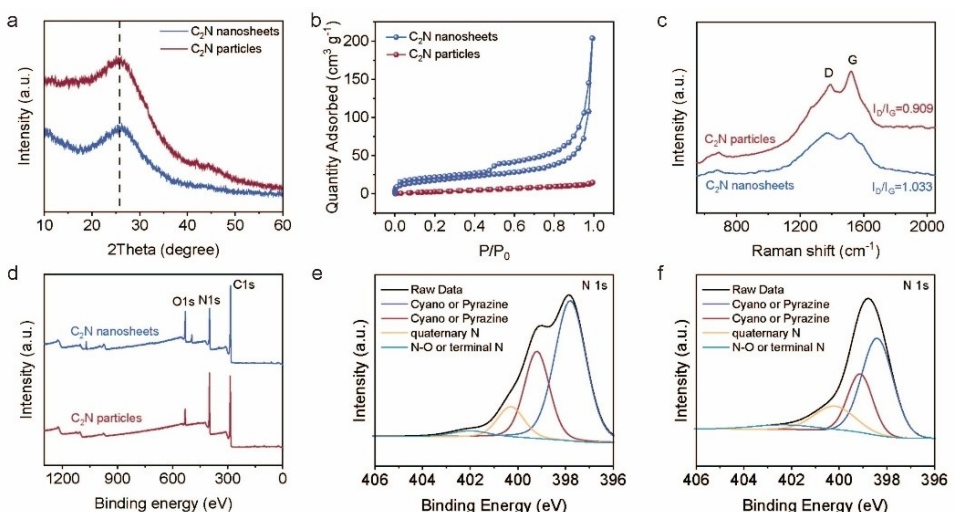


**Figure 2.** Characterization of pore structure and composition of  $\text{C}_2\text{N}$  nanosheets and  $\text{C}_2\text{N}$  particles. a)XRD patterns. b) Nitrogen adsorption-desorption isotherms. c) Raman survey spectra. d) XPS spectra of  $\text{C}_2\text{N}$  nanosheets and  $\text{C}_2\text{N}$  particles. e) Fitted N 1s XPS line scans of  $\text{C}_2\text{N}$  nanosheets. f) Fitted N 1s XPS line scans of  $\text{C}_2\text{N}$  particles.

advantageous to supply more sodium ion adsorption sites. In addition, due to the two-dimensional ultrathin structure of the  $\text{C}_2\text{N}$  nanosheets, the  $\text{C}_2\text{N}$  nanosheets expose more pores, which accelerates the fast transport of sodium ions (Figure S4, SI). The degree of graphitization is further analyzed by the Raman spectra. Figure 2c shows the Raman spectra of  $\text{C}_2\text{N}$  nanosheets and  $\text{C}_2\text{N}$  particles, which indicate the disordered  $\text{sp}^2$  carbon (D-peak) and graphitic  $\text{sp}^2$  carbon (G-peak), near  $1392\text{ cm}^{-1}$  and  $1526\text{ cm}^{-1}$ . The  $I_{\text{D}}/I_{\text{G}}$  intensity ratio of  $\text{C}_2\text{N}$  nanosheets is 1.272, which is higher than that of  $\text{C}_2\text{N}$  particles (1.036), implying the presence of more disordered morphologies and defects, thus providing sufficient active sites for Na ion binding.<sup>[22,28]</sup> In addition, the chemical compositions of  $\text{C}_2\text{N}$  nanosheets and  $\text{C}_2\text{N}$  particles are analyzed using X-ray photoelectron spectroscopy (XPS) (Figure 2d and S5, SI). Figure 2d shows the peaks corresponding to C 1s, N 1s, and O 1s of  $\text{C}_2\text{N}$  nanosheets and particles, which are located at 284.1 eV, 398.1 eV, and 531.1 eV, respectively.<sup>[44]</sup> Fitted C 1s XPS line scans of  $\text{C}_2\text{N}$  nanosheets and  $\text{C}_2\text{N}$  particles (Figure S5, SI) show that the peak at 283.8 eV corresponds to graphitized carbons. The two peaks at 284.8 eV and 287.0 eV belong to carbon bonded to  $\text{sp}^2$  hybridized nitrogen atoms. The peak around 289.0 eV corresponds to oxidized carbon atoms.<sup>[44]</sup> The N 1s region of  $\text{C}_2\text{N}$  nanosheets and  $\text{C}_2\text{N}$  particles can be fitted to four peaks in Figure 2e, f. The two peaks at 397.8 eV and 399.2 eV correspond to cyano and pyrazine nitrogen, and the peaks at 400.3 eV and 402.0 eV correspond to quaternary nitrogen atoms and nitrogen oxide, respectively. The nitrogen configuration plays a critical role in the structure and activity of the material.  $\text{C}_2\text{N}$  nanosheets contain more cyano and pyrazine nitrogen (86.3%) in all nitrogen configurations than  $\text{C}_2\text{N}$  particles (78.2%), which is beneficial to the adsorption of sodium ions.<sup>[40]</sup> Given this, the terrific structural feature of  $\text{C}_2\text{N}$  nanosheets would contribute to achieving prominent electrochemical performance.

To investigate the electrochemical performance of  $\text{C}_2\text{N}$  nanosheets, we assembled coin cells using prepared  $\text{C}_2\text{N}$  nanosheets and  $\text{C}_2\text{N}$  particles. Both  $\text{C}_2\text{N}$  nanosheets and  $\text{C}_2\text{N}$  particles have been fabricated as the anode for SIBs, and sodium tablets serve as cathodes. The electrochemical performances were first assessed by cyclic voltammetry (CV) analysis over a potential window between 0.01 and 3.00 V vs  $\text{Na}^+/\text{Na}$ , where the scanning rate is  $0.2\text{ mVs}^{-1}$ . The initial cycle of the CV curve of  $\text{C}_2\text{N}$  nanosheets is demonstrated in Figure 3a. In the initial cycle, there are three reduction peaks located around 0.02, 0.31, and 0.86 V. The peak at 0.86 V is attributed to the reaction of sodium ions with cyano and pyrazine nitrogen functional groups.<sup>[41]</sup> A reduction peak appears near 0.31 V but disappears on subsequent cycles, which can be ascribed to the formation of an irreversible Solid Electrolyte Interface film by the parasitic reaction at the electrode/electrolyte interface.<sup>[21]</sup> The peak located at 0.02 V is due to reversible sodium ions insertion into  $\text{C}_2\text{N}$  nanosheets. Figure S6, SI illustrates the CV curves of  $\text{C}_2\text{N}$  particles at  $0.2\text{ mVs}^{-1}$  within a potential window of 0.01 to 3.00 V (vs.  $\text{Na}^+/\text{Na}$ ), showing general agreement with  $\text{C}_2\text{N}$  nanosheets. The  $\text{C}_2\text{N}$  nanosheets show a discharging capacity of  $1148.7\text{ mAh g}^{-1}$  in the first cycle and an invertible capacity of  $389.8\text{ mAh g}^{-1}$  in the third cycle (Figure 3b). It can also be seen that the positions of the redox peaks are generally consistent with the Galvanostatic charge-discharge profile trends in the curves.<sup>[45]</sup> As manifested in Figure 3c, the rate performance of  $\text{C}_2\text{N}$  nanosheets has been tested at different current densities.  $\text{C}_2\text{N}$  nanosheets deliver high reversible capacities of 393.7, 327.8, 284.2, and  $265.8\text{ mAh g}^{-1}$  at 0.25, 0.5, 1.0, and  $1.5\text{ Ag}^{-1}$ , respectively. Remarkably, even at a high current density of  $2.0\text{ Ag}^{-1}$ ,  $\text{C}_2\text{N}$  nanosheets still achieve a stable capacity of  $255.4\text{ mAh g}^{-1}$ . In comparison,  $\text{C}_2\text{N}$  particles exhibit reversible capacities of 238.0, 201.9, 178.6, and  $165.4\text{ mAh g}^{-1}$  at 0.25, 0.5, 1.0, and  $1.5\text{ Ag}^{-1}$ , respectively. Only a capacity of  $154.6\text{ mAh g}^{-1}$  has been obtained at the current density of

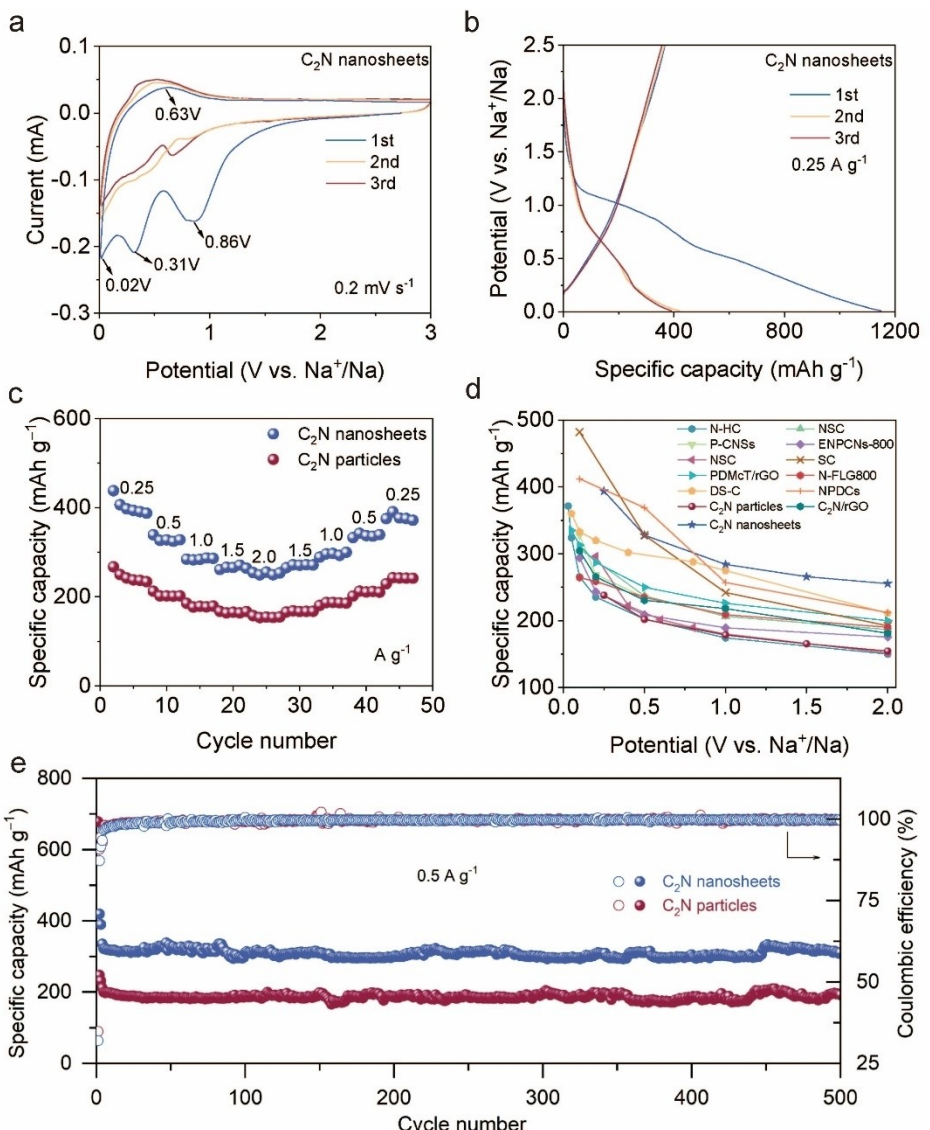


**Figure 3.** Electrochemical performance of  $\text{C}_2\text{N}$  nanosheets as SIB anodes in half cells. a) CV curves of  $\text{C}_2\text{N}$  nanosheets at a scan rate of  $0.2 \text{ mV s}^{-1}$  within a potential window of  $0.01\sim3.00 \text{ V}$  vs.  $\text{Na}^+/\text{Na}$ . b) Galvanostatic charge-discharge profiles of  $\text{C}_2\text{N}$  nanosheets at the current density of  $0.25 \text{ A g}^{-1}$ . c) Rate performance comparison of  $\text{C}_2\text{N}$  nanosheets and  $\text{C}_2\text{N}$  particles. d) Comparison of the rate performance between our  $\text{C}_2\text{N}$  nanosheets and other reported carbon-based materials for SIBs anode. e) Cycle performance comparison of  $\text{C}_2\text{N}$  nanosheets and  $\text{C}_2\text{N}$  particles at  $0.5 \text{ A g}^{-1}$ .

$2.0 \text{ A g}^{-1}$ . Evidently, due to the large number of effective active sites, and short ionic transport paths,  $\text{C}_2\text{N}$  nanosheets with outstanding rate capability outperform  $\text{C}_2\text{N}$  particles. The excellent rate property of  $\text{C}_2\text{N}$  nanosheets is competitive with many reported carbon-based materials in the literature for SIBs anode as demonstrated in Figure 3d.<sup>[21-23,26,41,46-51]</sup> Meanwhile,  $\text{C}_2\text{N}$  nanosheets also show a high discharge capacity of  $335.1 \text{ mAh g}^{-1}$  at the current density of  $0.5 \text{ A g}^{-1}$  and deliver a reversible capacity of  $311.0 \text{ mAh g}^{-1}$  after 500 cycles, maintaining a Coulombic efficiency of 99.7%. By contrast, the capacity of the  $\text{C}_2\text{N}$  particles only shows a discharge capacity of  $211.5 \text{ mAh g}^{-1}$  at  $0.5 \text{ A g}^{-1}$  and maintains at  $192.7 \text{ mAh g}^{-1}$  after 500 cycles in Figure 3e. It is precisely because  $\text{C}_2\text{N}$  nanosheets possess more effective nitrogen active sites and shorter ionic transport paths compared to  $\text{C}_2\text{N}$  particles, which facilitates the

storage and transport of sodium ions, thus demonstrating better sodium ion storage performance.

To gain a deeper understanding of the reasons why  $\text{C}_2\text{N}$  nanosheet electrodes exhibit excellent sodium storage performance, their electrochemical kinetic behavior has been studied. In the CV tests, the relationship between current ( $i$ ) and scan rate ( $v$ ) can be expressed by the equation.

$$i = av^b \quad (1)$$

where  $a$  and  $b$  are constant values. The  $b$ -value of 0.5 indicates a semi-infinite diffusion-controlled process, while the  $b$ -value of 1.0 represents a capacitive-controlled behavior.<sup>[21]</sup> Figure 4a tests the CV curves of  $\text{C}_2\text{N}$  nanosheets at scan rates of 0.2, 0.4, 0.6, 0.8, and 1.0  $\text{mV s}^{-1}$ . With the increase in scanning rate, the

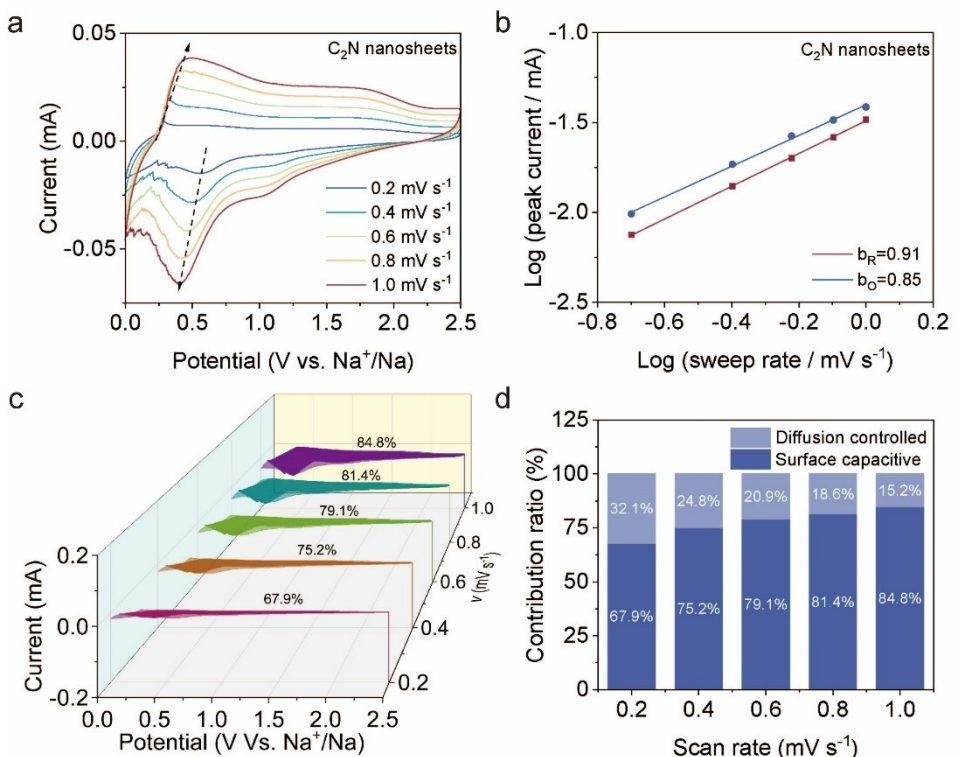


**Figure 4.** a) CV curves of  $\text{C}_2\text{N}$  nanosheets at various scan rates from 0.2 to 1.0  $\text{mV s}^{-1}$ . b) Corresponding linear fits of the peak current of CV curves of  $\text{C}_2\text{N}$  nanosheets. c, d) The pseudocapacitive and diffusion-controlled charge storage contributions at different scan rates of  $\text{C}_2\text{N}$  nanosheets.

reduction peak and oxidation peak shift to the direction of low potential and high potential, respectively, which may be due to electrode polarization or diffusion limitation as the scan rate increases. As displayed in Figure 4b and S8, the  $b$ -values of the reduction peak and oxidation peak are 0.91 and 0.85 for  $\text{C}_2\text{N}$  nanosheets, which exceed those of  $\text{C}_2\text{N}$  particles (0.85 and 0.81), implying that  $\text{C}_2\text{N}$  nanosheets are more favorable for  $\text{Na}^+$  ion diffusion. In comparison, the pseudocapacitive behavior of  $\text{C}_2\text{N}$  nanosheets plays a more significant role than  $\text{C}_2\text{N}$  particles in sodium ion storage. Figure 4c demonstrates the fitted CV curves at different scan rates, where the shaded area represents the pseudo-capacitance contribution. As the scan rate increases from 0.2 to 1.0  $\text{mV s}^{-1}$ , the pseudo-capacitance contributions ratio for  $\text{C}_2\text{N}$  nanosheets improves from 67.9% to 84.8%, which agrees with the sloped contours of the charge-discharge curves. The surface pseudo-capacitance contribution dominates over the diffusion-controlled contribution (Figure 4d). The highest pseudo-capacitance contribution of  $\text{C}_2\text{N}$  particles at 1.0  $\text{mV s}^{-1}$  is only 81.9%. Given the enhanced pseudo-capacitance contribution,  $\text{C}_2\text{N}$  nanosheets show enhanced sodium ion storage kinetics and excellent rate performance. The mainly capacitance-controlled sodium ion storage mechanism of  $\text{C}_2\text{N}$  nanosheets should be attributed to the fact that  $\text{C}_2\text{N}$  nanosheets have more exposed effective nitrogen active sites and shorter ion transport paths.

Figure 5a, b shows the galvanostatic charge-discharge profiles of  $\text{C}_2\text{N}$  nanosheets and  $\text{C}_2\text{N}$  particles at different current densities. In comparison, the  $\text{C}_2\text{N}$  nanosheets show more stable

discharge/charge profiles with increasing current density.  $\text{C}_2\text{N}$  nanosheets demonstrate less polarization than  $\text{C}_2\text{N}$  particles, indicating excellent  $\text{Na}^+$  storage reaction kinetics.<sup>[47]</sup> At a voltage of about 0.5 V,  $\text{C}_2\text{N}$  nanosheets provide more sodium storage capacity than  $\text{C}_2\text{N}$  particles. With the increase of current density, the plateau capacity of  $\text{C}_2\text{N}$  nanosheets gradually decreases from 163.1  $\text{mAh g}^{-1}$  to 125.7  $\text{mAh g}^{-1}$ , compared to that of  $\text{C}_2\text{N}$  particles, which decreases from 90.4  $\text{mAh g}^{-1}$  to 56.8  $\text{mAh g}^{-1}$ . Besides, the lower sodium storage voltage of the anode material (0~0.1 V) may lead to sodium dendrites during full cell overcharging. In contrast, the appropriate sodium storage voltage of  $\text{C}_2\text{N}$  nanosheets can inhibit the formation of dendrites, thus ensuring safer and more stable storage of  $\text{Na}^+$  ions.<sup>[52]</sup> Besides, long cycling performance has been performed at a current density of 2  $\text{A g}^{-1}$  to further test the stability of  $\text{C}_2\text{N}$  nanosheets. In Figure 5c,  $\text{C}_2\text{N}$  nanosheets retain reversible capacity retention of 92.9%. After 1500 cycles at 2.0  $\text{A g}^{-1}$ ,  $\text{C}_2\text{N}$  nanosheets still obtained a reversible specific capacity of 232.1  $\text{mAh g}^{-1}$ , which is superior to that of  $\text{C}_2\text{N}$  particles (147.1  $\text{mAh g}^{-1}$ ). In addition, the performance of  $\text{C}_2\text{N}$  nanosheets also surpasses that of  $\text{C}_2\text{N}/\text{rGO}$  (218.8  $\text{mAh g}^{-1}$  at 1.0  $\text{A g}^{-1}$  after 1000 cycles).<sup>[41]</sup> Table S2 of the Supporting Information compares the cycling performance of  $\text{C}_2\text{N}$  nanosheets with other reported carbon-based materials for SIBs anode.  $\text{C}_2\text{N}$  nanosheets show excellent cycling stability compared to other carbon-based materials.

To further evaluate the structural stability of two electrodes, the Electrochemical impedance spectra (EIS) of  $\text{C}_2\text{N}$  nanosheets

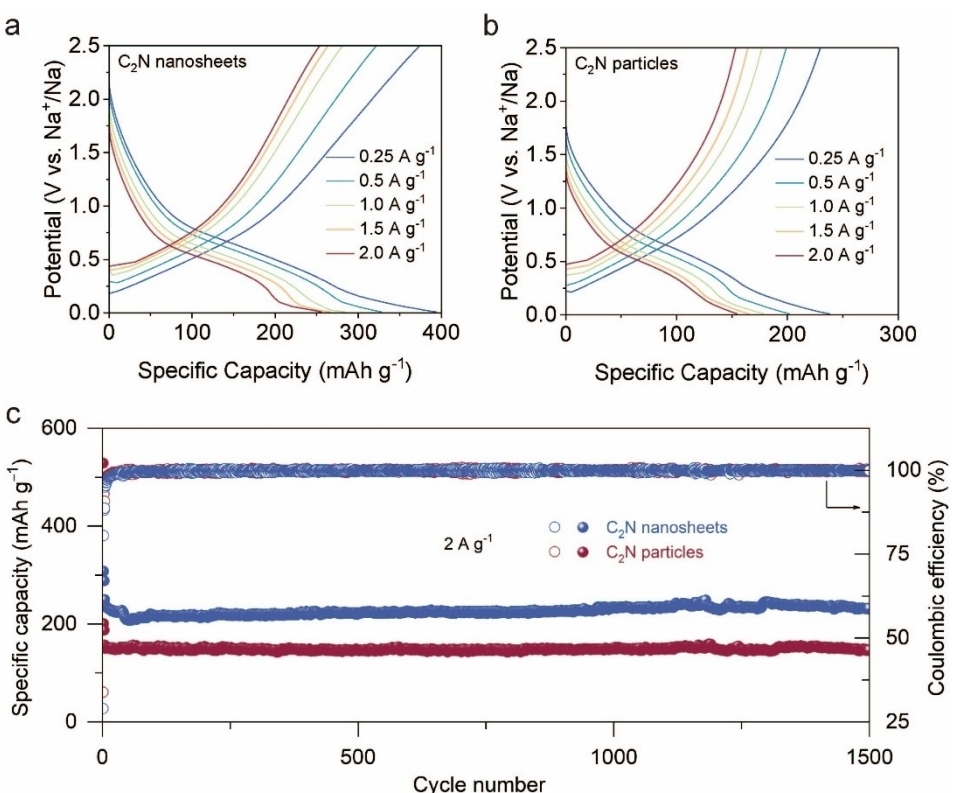


**Figure 5.** Galvanostatic charge-discharge profiles of a)  $\text{C}_2\text{N}$  nanosheets and b)  $\text{C}_2\text{N}$  particles at various rates. c) Long cycling performance of  $\text{C}_2\text{N}$  nanosheets and  $\text{C}_2\text{N}$  particles at a current density of  $2 \text{ A g}^{-1}$ .

and  $\text{C}_2\text{N}$  particles have been measured before and after cycling (Figure S9 and S10, SI). The Nyquist plots show that the impedance value of  $\text{C}_2\text{N}$  nanosheets is slightly lower than that of  $\text{C}_2\text{N}$  particles before cycling. After the electrochemical activation process, the activity of electrodes is improved and the impedance values of both are reduced.<sup>[53]</sup> After 100 cycles, the impedance values of both change little, while the impedance value of  $\text{C}_2\text{N}$  nanosheets remains lower than that of  $\text{C}_2\text{N}$  particles. These results demonstrate that the  $\text{C}_2\text{N}$  nanosheets have a stable structure during cycling. Due to the higher specific area and more active sites for sodium ion storage,  $\text{C}_2\text{N}$  nanosheets have a larger contact area with the electrolyte, which accelerates the transport of electrons and ions across the electrode/electrolyte interface.

## Conclusions

In summary, our research has demonstrated exceptional advancements in the reversible storage capacity and sustained cycling stability of sodium ion storage through the utilization of two-dimensional ultrathin large-area  $\text{C}_2\text{N}$  nanosheets. The  $\text{C}_2\text{N}$  nanosheets, featuring abundant effective nitrogen-active sites, were prepared by chemical vapor deposition employing salt templates.  $\text{C}_2\text{N}$  nanosheets exhibit superior sodium storage characteristics, including high reversible capacity, impressive rate property, and sustained cycling performance. The electro-

chemical analysis underscores the critical role of pseudo-capacitive behavior in driving the excellent performance of  $\text{C}_2\text{N}$  anodes. This research introduces a promising pathway for the development of carbon-based anodes capable of delivering both excellent capacity and exceptional stability in sodium-ion battery applications.

## Experimental Section

### Materials

1,4,5,8,9,11-Hexaazatriphenylenehexacarbonitrile (HAT-CN) was obtained from Shanghai Macklin Biochemical Co., Ltd. Sodium chloride was provided from Shanghai Bide Medical Technology Co., Ltd. Dichloromethane and Ethanol were supplied from Shanghai LingFeng Chemical Reagents Co., Ltd.

### Synthesis of $\text{C}_2\text{N}$ nanosheets

The  $\text{C}_2\text{N}$  nanosheets were synthesized through a salt-templated method. Typically, 100 mg of HAT-CN was dispersed in 10 ml of dichloromethane with magnetic stirring for 20 minutes. Then, The precursor dispersion was mixed with 600 g of NaCl crystals with continuous manual shaking and dried at 80 °C. After that, the mixture of HAT-CN and NaCl was heated in a tube furnace. Argon at a flow rate of 100  $\text{ml min}^{-1}$  was used as a protective gas. The temperature was raised from 25 °C to 550 °C for 120 minutes and then kept at 550 °C for 120 minutes. Finally, the obtained product

was washed with numerous deionized water several times to remove the sodium chloride completely. The floated C<sub>2</sub>N nanosheets were collected before being freeze-dried for 48 hours for further characterization.

### Synthesis of C<sub>2</sub>N particles

The C<sub>2</sub>N particles were synthesized using a previously reported method.<sup>[44,54]</sup> HAT-CN (300 mg) was annealed in a tube furnace. Argon at a flow rate of 100 ml min<sup>-1</sup> was used as a protective gas. The temperature was raised from 25 °C to 550 °C for 120 minutes and then kept at 550 °C for 120 minutes. The resulting material was named C<sub>2</sub>N particles.

### Coin cells assembly and electrochemical performance measurements

The electrochemical measurements of half-cells were performed by using CR2032 coin cells at 25 °C. All cells were assembled in an Ar-filled glove box with the content of H<sub>2</sub>O and O<sub>2</sub> below 0.01 ppm. The LAND test system was used to perform charge-discharge tests at different current densities in a voltage window of 0.01 to 2.50 V versus Na<sup>+</sup>/Na. at room temperature. All cycle tests were performed after activating the battery for three cycles at 0.25 Ag<sup>-1</sup>. The CV was measured using an electrochemical workstation (Chenhua Instrument, CHI760E). Sodium tablets served as reference and counter electrodes. Glass fiber was utilized as the separator. Working electrodes were obtained by mixing C<sub>2</sub>N nanosheets or C<sub>2</sub>N particles, Super P, and polyvinylidene fluoride (PVDF) with a mass ratio of 7:2:1 in N-methyl-pyrrolidone (NMP). After mixing for 12 h, the uniform slurry was coated on Cu foil and then vacuum dried at 120 °C overnight. The mass loading of C<sub>2</sub>N nanosheets or C<sub>2</sub>N particles for each anode was found to be about 1 mg cm<sup>-2</sup>. 1 M NaClO<sub>4</sub> in a mixture of ethylene carbonate (EC) and dimethyl carbonate (DMC) (1:1, v/v) with 2% fluoroethylene carbonate (FEC) served as an electrolyte.

### Materials characterizations

The shape and morphology of C<sub>2</sub>N nanosheets and C<sub>2</sub>N particles were observed by scanning electron microscopy (SEM, FEI Inspect F50) and transmission electron microscopy (TEM, Talos-F200X). The element mappings were tested using energy dispersive spectrometry connected with SEM. The morphology and thickness of C<sub>2</sub>N nanosheets were observed using Atomic force microscopy (AFM, Bruker Dimension Icon Atomic Force Microscope). The N<sub>2</sub> adsorption and desorption isotherms were performed at 77.3 K (Micromeritics ASAP 2020 HD88), and the pore size distributions were acquired by the Barrett-Joyner-Halenda (BJH) method. X-ray diffraction (XRD) patterns were obtained on a Rigaku Smartlab X-ray diffractometer (Cu K $\alpha$ ,  $\lambda=1.5406\text{ \AA}$ ). X-ray photoelectron spectroscopy (XPS) data was recorded using an ESCALAB 250 XI (Thermo Kalpha) with the mono Al K $\alpha$ . Raman spectra were determined by a LabRAM HR UV-visible Raman Microprobe.

### Supporting Information

Supporting Information is available from the Wiley Online Library or from the author.

### Acknowledgements

The authors acknowledge the financial support from the National Key Research and Development Program of China (2022YFB3807200) and the National Natural Science Foundations of China (22371041).

### Conflict of Interests

The authors declare no conflict of interest.

### Data Availability Statement

Research data are not shared.

**Keywords:** anode materials · ultrathin C<sub>2</sub>N nanosheets · sodium-ion storage · electrochemistry

- [1] T. Liu, Y. Zhang, Z. Jiang, X. Zeng, J. Ji, Z. Li, X. Gao, M. Sun, Z. Lin, M. Ling, J. Zheng, C. Liang, *Energy Environ. Sci.* **2019**, *12*, 1512–1533.
- [2] P. K. Nayak, L. Yang, W. Brehm, P. Adelhelm, *Angew. Chem. Int. Ed.* **2018**, *57*, 102–120.
- [3] Z. Zhang, Y. Du, Q.-C. Wang, J. Xu, Y.-N. Zhou, J. Shen, X. Zhou, *Angew. Chem. Int. Ed.* **2020**, *59*, 17504–17510.
- [4] W. Zhang, M. Sun, J. Yin, W. Wang, G. Huang, X. Qiu, U. Schwingenschlögl, H. N. Alshareef, *Nano Energy* **2021**, *87*, 106184.
- [5] J.-Y. Hwang, S.-T. Myung, Y.-K. Sun, *Chem. Soc. Rev.* **2017**, *46*, 3529–3614.
- [6] R. Usiskin, Y. Lu, J. Popovic, M. Law, P. Balaya, Y.-S. Hu, J. Maier, *Nat. Rev. Mater.* **2021**, *6*, 1020–1035.
- [7] C. Chen, Y. Huang, Y. Zhu, Z. Zhang, Z. Guang, Z. Meng, P. Liu, *ACS Sustainable Chem. Eng.* **2020**, *8*, 1497–1506.
- [8] G. Kothandam, G. Singh, X. Guan, J. M. Lee, K. Ramadass, S. Joseph, M. Benigar, A. Karakoti, J. Yi, P. Kumar, A. Vinu, *Adv. Sci.* **2023**, *10*, 2301045.
- [9] H. Tan, D. Chen, X. Rui, Y. Yu, *Adv. Funct. Mater.* **2019**, *29*, 1808745.
- [10] Y. Zheng, S. Wei, J. Shang, D. Wang, C. Lei, Y. Zhao, *Small* **2023**, *23*03746.
- [11] N. Zhang, X. Han, Y. Liu, X. Hu, Q. Zhao, J. Chen, *Adv. Energy Mater.* **2015**, *5*, 1401123.
- [12] J. Ni, S. Fu, C. Wu, Y. Zhao, J. Maier, Y. Yu, L. Li, *Adv. Energy Mater.* **2016**, *6*, 1502568.
- [13] E. Goikolea, V. Palomares, S. Wang, I. R. De Larramendi, X. Guo, G. Wang, T. Rojo, *Adv. Energy Mater.* **2020**, *10*, 2002055.
- [14] Y. Xu, M. Zhou, Y. Lei, *Mater. Today* **2018**, *21*, 60–78.
- [15] Q. Wang, C. Zhao, Y. Lu, Y. Li, Y. Zheng, Y. Qi, X. Rong, L. Jiang, X. Qi, Y. Shao, D. Pan, B. Li, Y. Hu, L. Chen, *Small* **2017**, *13*, 1701835.
- [16] L. Zhao, Z. Hu, W. Lai, Y. Tao, J. Peng, Z. Miao, Y. Wang, S. Chou, H. Liu, S. Dou, *Adv. Energy Mater.* **2021**, *11*, 2002704.
- [17] K. Schutjajew, P. Giusto, E. Härk, M. Oschatz, *Carbon* **2021**, *185*, 697–708.
- [18] P. Li, Y. Shen, X. Li, W. Huang, X. Lu, *Energy Environ. Mater.* **2022**, *5*, 608–616.
- [19] X. Xia, H. Yin, Y. Zhang, S. Huang, *Surf. Interfaces* **2023**, *36*, 102479.
- [20] C. Sathish, G. Kothandam, P. Selvarajan, Z. Lei, J. Lee, J. Qu, A. H. Al-Muhtaseb, X. Yu, M. B. H. Breese, R. Zheng, J. Yi, A. Vinu, *Adv. Sci.* **2022**, *9*, 2105603.
- [21] C. Xu, W. Yang, G. Ma, S. Che, Y. Li, Y. Jia, N. Chen, G. Huang, Y. Li, *Small* **2022**, *18*, 2204375.
- [22] X. Hu, X. Sun, S. J. Yoo, B. Evanko, F. Fan, S. Cai, C. Zheng, W. Hu, G. D. Stucky, *Nano Energy* **2019**, *56*, 828–839.
- [23] H. Hou, L. Shao, Y. Zhang, G. Zou, J. Chen, X. Ji, *Adv. Sci.* **2017**, *4*, 1600243.
- [24] W. Liu, L. Du, S. Ju, X. Cheng, Q. Wu, Z. Hu, X. Yu, *ACS Nano* **2021**, *15*, 5679–5688.
- [25] K. Wu, Y. Feng, Y. Xie, J. Zhang, D. Xiong, L. Chen, Z. Feng, K. Wen, M. He, *J. Alloys Compd.* **2023**, *938*, 168430.

- [26] X. Xu, H. Zeng, D. Han, K. Qiao, W. Xing, M. J. Rood, Z. Yan, *ACS Appl. Mater. Interfaces* **2018**, *10*, 37172–37180.
- [27] B. Yin, S. Liang, D. Yu, B. Cheng, I. L. Egun, J. Lin, X. Xie, H. Shao, H. He, A. Pan, *Adv. Mater.* **2021**, *33*, 2100808.
- [28] Y. Yuan, Z. Chen, H. Yu, X. Zhang, T. Liu, M. Xia, R. Zheng, M. Shui, J. Shu, *Energy Storage Mater.* **2020**, *32*, 65–90.
- [29] S. Zhao, Z. Guo, J. Yang, C. Wang, B. Sun, G. Wang, *Small* **2021**, *17*, 2007431.
- [30] Y. Li, M. Chen, B. Liu, Y. Zhang, X. Liang, X. Xia, *Adv. Energy Mater.* **2020**, *10*, 2000927.
- [31] Y. Fu, C. Zhu, *Acta Phys.-Chim. Sin.* **2023**, *39*, 2209002.
- [32] Y. Tang, X. Wang, J. Chen, X. Wang, D. Wang, Z. Mao, *Carbon* **2021**, *174*, 98–109.
- [33] M. Chen, L. Zhou, T. Wang, H. Xia, H. Liu, S. Dou, S. Chou, *Adv. Funct. Mater.* **2023**, *33*, 2214786.
- [34] H. Wang, Z. Wu, F. Meng, D. Ma, X. Huang, L. Wang, X. Zhang, *ChemSusChem* **2013**, *6*, 56–60.
- [35] Z. Tian, N. López-Salas, C. Liu, T. Liu, M. Antonietti, *Adv. Sci.* **2020**, *7*, 2001767.
- [36] L. Tan, C. Nie, Z. Ao, H. Sun, T. An, S. Wang, *J. Mater. Chem. A* **2021**, *9*, 17–33.
- [37] N. López-Salas, J. Albero, *Front. Mater.* **2021**, *8*, 772200.
- [38] J. Xu, J. Mahmood, Y. Dou, S. Dou, F. Li, L. Dai, J. Baek, *Adv. Mater.* **2017**, *29*, 1702007.
- [39] T. Hussain, D. J. Searles, M. Hankel, *Carbon* **2020**, *160*, 125–132.
- [40] D. Wu, B. Yang, H. Chen, E. Ruckenstein, *Energy Storage Mater.* **2019**, *16*, 574–580.
- [41] T. Guo, P. Chen, L. Liu, J. Ma, J. Sun, Y. Ding, J. Xu, Y. Song, H. Chen, X. Ouyang, X. Wang, J. Zhu, Y. Fu, *ACS Sustainable Chem. Eng.* **2021**, *9*, 15946–15956.
- [42] X. Sheng, Z. Zhang, T. Ding, J. Liao, X. Zhou, *Chem. J. Chin. Univ.* **2023**, *44*, 20220724.
- [43] J. Mahmood, E. K. Lee, M. Jung, D. Shin, I.-Y. Jeon, S.-M. Jung, H.-J. Choi, J.-M. Seo, S.-Y. Bae, S.-D. Sohn, N. Park, J. H. Oh, H.-J. Shin, J.-B. Baek, *Nat. Commun.* **2015**, *6*, 6486.
- [44] R. Walczak, B. Kurpil, A. Savateev, T. Heil, J. Schmidt, Q. Qin, M. Antonietti, M. Oschatz, *Angew. Chem. Int. Ed.* **2018**, *57*, 10765–10770.
- [45] J. Zou, K. Fan, X. Wang, Y. Chen, Y. Cao, H. Dai, C. Zhang, M. Fu, Y. Gao, H. Liu, C. Wang, *Chem. Eng. J.* **2023**, *460*, 141703.
- [46] S. Tao, W. Xu, J. Zheng, F. Kong, P. Cui, D. Wu, B. Qian, S. Chen, L. Song, *Carbon* **2021**, *178*, 233–242.
- [47] J. Li, Z. Ding, L. Pan, J. Li, C. Wang, G. Wang, *Carbon* **2021**, *173*, 31–40.
- [48] Y. Li, W. Zhong, C. Yang, F. Zheng, Q. Pan, Y. Liu, G. Wang, X. Xiong, M. Liu, *Chem. Eng. J.* **2019**, *358*, 1147–1154.
- [49] J. Liu, Y. Zhang, L. Zhang, F. Xie, A. Vasileff, S. Qiao, *Adv. Mater.* **2019**, *31*, 1901261.
- [50] L. Qie, W. Chen, X. Xiong, C. Hu, F. Zou, P. Hu, Y. Huang, *Adv. Sci.* **2015**, *2*, 201500195.
- [51] W. Li, M. Zhou, H. Li, K. Wang, S. Cheng, K. Jiang, *Energy Environ. Sci.* **2015**, *8*, 2916–2921.
- [52] Z. Tian, Y. Zhang, J. Zhu, Q. Li, T. Liu, M. Antonietti, *Adv. Energy Mater.* **2021**, *11*, 2102489.
- [53] D. Zhang, J. Lu, C. Pei, S. Ni, *Adv. Energy Mater.* **2022**, *12*, 2103689.
- [54] L. Tan, J. Wang, B. Cai, C. Wang, Z. Ao, S. Wang, *J. Hazard. Mater.* **2022**, *424*, 127348.

Manuscript received: December 27, 2023

Revised manuscript received: January 31, 2024

Accepted manuscript online: February 1, 2024

Version of record online: February 20, 2024